Prediction of deformation and hygro-thermal stresses distribution in PEM fuel cell vehicle using three-dimensional CFD model

Maher A.R. Sadiq Al-Baghdadi

Fuel Cell Research Center, International Energy & Environment Foundation, Al-Najaf, P.O.Box 39, Iraq.

Abstract
Durability is one of the most critical remaining issues impeding successful commercialization of broad PEM fuel cell transportation energy applications. Automotive fuel cells are likely to operate with neat hydrogen under load-following or load-levelled modes and be expected to withstand variations in environmental conditions, particularly in the context of temperature and atmospheric composition. In addition, they are also required to survive over the course of their expected operational lifetimes i.e., around 5,500 hrs, while undergoing as many as 30,000 startup/shutdown cycles. The damage mechanisms in a PEM fuel cell are accelerated by mechanical stresses arising during fuel cell assembly (bolt assembling), and the stresses arise during fuel cell running, because it consists of the materials with different thermal expansion and swelling coefficients. Therefore, in order to acquire a complete understanding of the damage mechanisms in the membrane, mechanical response under steady-state hygro-thermal stresses should be studied under real cell operating conditions and in real cell geometry (three-dimensional). In this work, full three-dimensional, non-isothermal computational fluid dynamics model of a PEM fuel cell has been developed to simulate the stresses inside the PEM fuel cell, which are occurring during fuel cell assembly (bolt assembling), and the stresses arise during fuel cell running due to the changes of temperature and relative humidity. A unique feature of the present model is to incorporate the effect of hygro and thermal stresses into actual three-dimensional fuel cell model. In addition, the temperature and humidity dependent material properties are utilize in the simulation for the membrane. The model is shown to be able to understand the many interacting, complex electrochemical, transport phenomena, and stresses distribution that have limited experimental data. This model is used to study and analyse the effect of operating parameters on the mechanical behaviour of PEM. The analysis helped identifying critical parameters and shed insight into the physical mechanisms leading to a fuel cell durability for vehicular applications.

Keywords: Fuel cell vehicles; PEM fuel cells, Durability, Hygro-thermal stress, CFD.

1. Introduction
The world's leading automakers, fuel cell developers, material and component suppliers, laboratories and universities are in a race to bring fuel cell vehicles (FCVs) to the marketplace. The goal of this pursuit is to offer an alternative to the internal combustion engine that provides all the performance consumers have come to demand, and at the same time is more efficient, environmentally friendly, increases our fuel diversity, and is ultimately less expensive to manufacture, maintain and operate.

For vehicular applications fuel cell systems need to be different from stationary power generation. Available space in vehicles is much more critical and fast response times and start-up times are required. Prototype fuel-cell-powered vehicles have recently been demonstrated by several car manufactures. All of the various demonstration vehicles are based on a basic conceptual design combining the proton exchange membrane (PEM) fuel cell with an electric drive. The PEM fule clee is regarded as ideally suited for transportation applications due to its high power density, high energy conversion efficiency, compactness, lightweight, and low-operating temperature (below 100 C). The recent PEM driven electric vehicles have demonstrated the technical feasibility of the concept. However, among all applications for fuel cells the transportation application involves the most stringent requirements regarding volumetric and gravimetric power density, reliability, and costs.

In an automotive PEM fuel cell, hydrogen and oxygen undergo a relatively cool, electrochemical reaction that directly produces electrical energy. This electricity would be used by motors, including one or more connected to axles used to power the wheels of the vehicle (Figure 1). The direct hydrogen fuel cell vehicle will have no emissions even during idling - this is especially important during city rush hours.
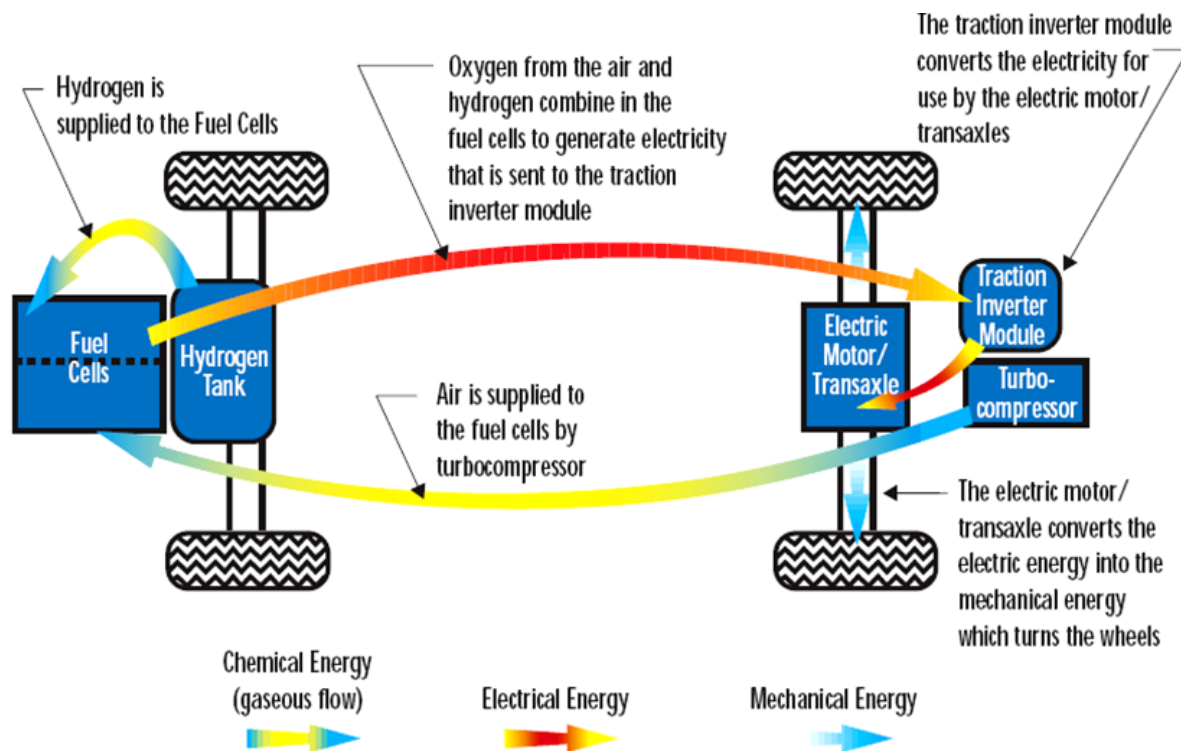
Figure 1. A zero-emission vehicle that utilizes a direct hydrogen polymer electrolyte fuel cell

Variations in operating modes and general cell design according to application means that how dominant certain performance degradation and failure mechanisms are also change according to application. Automotive fuel cells, for example, are likely to operate with neat hydrogen under loadfollowing or load-levelled modes and be expected to withstand variations in environmental conditions, particularly in the context of temperature and atmospheric composition. In addition, they are also required to survive over the course of their expected operational lifetimes i.e., around 5,500 hrs, while undergoing as many as 30,000 startup/shutdown cycles. PEFCs for stationary applications would not be subjected to as many startup/shutdown cycles, however, would be expected to survive up to 10,000 - 40,000 hrs of operation whilst maintaining a tolerance to fuel impurities in the reformate feed.

Durability is one of the most critical remaining issues impeding successful commercialization of broad PEM fuel cell transportation energy applications, and the durability of fuel cell stack components remains, in most cases, insufficiently understood. Lengthy required testing times, lack of understanding of most degradation mechanisms, and the difficulty of performing in-situ, non-destructive structural evaluation of key components makes the topic a difficult one [1, 2].

The Membrane-Electrode-Assembly (MEA) is the core component of PEM fuel cell and consists of membrane with the gas-diffusion layers including the catalyst attached to each side. The fuel cell MEA durability plays a vital role in the overall lifetime achieved by a stack in field applications. Within the MEA's electrocatalyst layers are three critical interfaces that must remain properly intermingled for optimum MEA performance: platinum/carbon interface (for electron transport and catalyst support); platinum/Nafion interface (for proton transport); and Nafion/carbon interface (for high-activity catalyst dispersion and structural integrity). The MEA performance shows degradation over operating time, which is dependent upon materials, fabrication and operating conditions [3-5].

Mechanical degradation is often the cause of early life failures. Mechanical damage in the PEM can appear as through-the-thickness flaws or pinholes in the membrane, or delaminating between the polymer membrane and gas diffusion layers [6, 7]. Mechanical stresses which limit MEA durability have two origins. Firstly, this is the stresses arising during fuel cell assembly (bolt assembling). The bolts provide the tightness and the electrical conductivity between the contact elements. Secondly, additional mechanical stresses occur during fuel cell running because PEM fuel cell components have different thermal expansion and swelling coefficients. Thermal and humidity gradients in the fuel cell produce dilatations obstructed by tightening of the screw-bolts. Compressive stress increasing with the hygro-thermal loading can exceed the yield strength which causes the plastic deformation. The mechanical behaviour of the membrane depends strongly on hydration and temperature [8-10].

Al-Baghdadi [11] incorporated the effect of hygro and thermal stresses into non-isothermal three-dimensional CFD model of PEM fuel cell to simulate the hygro and thermal stresses in one part of the fuel cell components, which is the polymer membrane.

An operating fuel cell has varying local conditions of temperature, humidity, and power generation (and thereby heat generation) across the active area of the fuel cell in three-dimensions. Nevertheless, except of ref. [11], no models have yet been published to incorporate the effect of hygro-thermal stresses into actual fuel cell models to study the effect of these real conditions on the stresses developed in membrane and gas diffusion layers. In addition, as a result of the architecture of a cell, the transport phenomena in a fuel cell are inherently three-dimensional, but no models have yet been published to address the hygro-thermal stresses in PEM fuel cells with three-dimensional effect. Suvorov et al. [12] reported that the error introduced due to two-dimensional assumption is about 10%. Therefore, in order to acquire a complete understanding of the damage mechanisms in the membrane and gas diffusion layers, mechanical response under steady-state hygro-thermal stresses should be studied under real cell operating conditions and in real cell geometry (three-dimensional).

The difficult experimental environment of fuel cell systems has stimulated efforts to develop models that could simulate and predict multi-dimensional coupled transport of reactants, heat and charged species using computational fluid dynamic (CFD) methods. A comprehensive computational model should include the equations and other numerical relations needed to fully define fuel cell behaviour over the range of interest. In the present work, full three-dimensional, non-isothermal computational fluid dynamics model of a PEM fuel cell has been developed to simulate the hygro and thermal stresses in PEM fuel cell, which are occurring during the cell operation due to the changes of temperature and relative humidity. The temperature and humidity dependent material properties are utilize in the simulation for the membrane. This model is used to study the effect of operating parameters on fuel cell performance and hygro-thermal stresses in the PEM fuel cell.

2. Model description

The present work presents a comprehensive three–dimensional, multi–phase, non-isothermal model of a PEM fuel cell that incorporates the significant physical processes and the key parameters affecting fuel cell performance. The model accounts for both gas and liquid phase in the same computational domain, and thus allows for the implementation of phase change inside the gas diffusion layers. The model includes the transport of gaseous species, liquid water, protons, and energy. Water transport inside the porous gas diffusion layer and catalyst layer is described by two physical mechanisms: viscous drag and capillary pressure forces, and is described by advection within the gas channels. Water transport across the membrane is also described by two physical mechanisms: electro-osmotic drag and diffusion. The model features an algorithm that allows for a more realistic representation of the local activation overpotentials, which leads to improved prediction of the local current density distribution. This leads to high accuracy prediction of temperature distribution in the cell and therefore thermal stresses. This model also takes into account convection and diffusion of different species in the channels as well as in the

porous gas diffusion layer, heat transfer in the solids as well as in the gases, and electrochemical reactions. The present multi-phase model is capable of identifying important parameters for the wetting behaviour of the gas diffusion layers and can be used to identify conditions that might lead to the onset of pore plugging, which has a detrimental effect of the fuel cell performance. A unique feature of the model is to incorporate the effect of hygro-thermal stresses into actual three-dimensional fuel cell model. This model is used to investigate the hygro and thermal stresses in PEM fuel cell, which developed during the cell operation due to the changes of temperature and relative humidity.

2.1 Computational domain
A computational model of an entire cell would require very large computing resources and excessively long simulation times. The computational domain in this study is therefore limited to one straight flow channel with the land areas. The full computational domain consists of cathode and anode gas flow channels, and the membrane electrode assembly as shown in Figure 2.
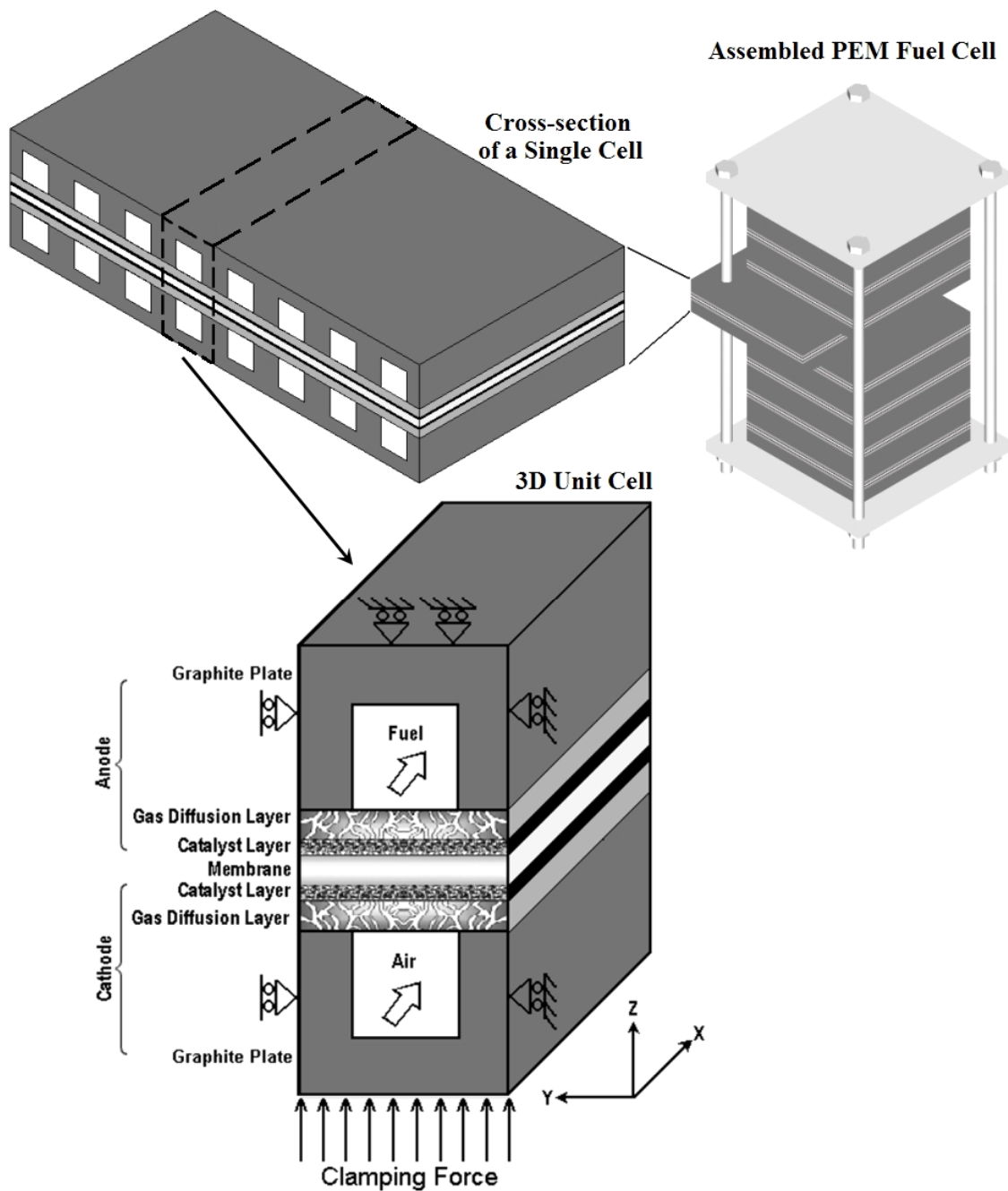
Figure 2. Three-dimensional computational domain

2.2 Model equations
2.2.1 Gas flow channels
In the fuel cell channels, the gas-flow field is obtained by solving the steady-state Navier-Stokes equations, i.e. the continuity equation, the mass conservation equation for each phase yields the volume fraction (r) and along with the momentum equations the pressure distribution inside the channels. The continuity equation for the gas phase inside the channel is given by;

$$\nabla \cdot \left(r_g \rho_g \mathbf{u}_g \right) = 0 \tag{1}$$

and for the liquid phase inside the channel becomes;

$$\nabla \cdot \left(r_l \rho_l \mathbf{u}_l \right) = 0 \tag{2}$$

where **u** is velocity vector [m/s], ρ is density [kg/m^3].

Two sets of momentum equations are solved in the channels, and they share the same pressure field. Under these conditions, it can be shown that the momentum equations becomes;

$$\nabla \cdot \left(\rho_g \mathbf{u}_g \otimes \mathbf{u}_g - \mu_g \nabla \mathbf{u}_g \right) = -\nabla r_g \left(P + \frac{2}{3} \mu_g \nabla \cdot \mathbf{u}_g \right) + \nabla \cdot \left[\mu_g \left(\nabla \mathbf{u}_g \right)^T \right] \tag{3}$$

$$\nabla \cdot \left(\rho_l \mathbf{u}_l \otimes \mathbf{u}_l - \mu_l \nabla \mathbf{u}_l \right) = -\nabla r_l \left(P + \frac{2}{3} \mu_l \nabla \cdot \mathbf{u}_l \right) + \nabla \cdot \left[\mu_l \left(\nabla \mathbf{u}_l \right)^T \right] \tag{4}$$

where P is pressure (Pa), μ is viscosity [kg/(m·s)].

The mass balance is described by the divergence of the mass flux through diffusion and convection. Multiple species are considered in the gas phase only, and the species conservation equation in multi-component, multi-phase flow can be written in the following expression for species i;

$$\nabla \cdot \left[\begin{array}{c} -r_g \rho_g y_i \sum_{j=1}^{N} D_{ij} \frac{M}{M_j} \left[\left(\nabla y_j + y_j \frac{\nabla M}{M} \right) + \left(x_j - y_j \right) \frac{\nabla P}{P} \right] + \\ r_g \rho_g y_i \cdot \mathbf{u}_g + D_i^T \frac{\nabla T}{T} \end{array} \right] = 0 \tag{5}$$

where T is temperature (K), y is mass fraction, x is mole fraction, D is diffusion coefficient [m^2/s]. Subscript i denotes oxygen at the cathode side and hydrogen at the anode side, and j is water vapour in both cases. Nitrogen is the third species at the cathode side.
The Maxwell-Stefan diffusion coefficients of any two species are dependent on temperature and pressure. They can be calculated according to the empirical relation based on kinetic gas theory [13];

$$D_{ij} = \frac{T^{1.75} \times 10^{-3}}{P \left[\left(\sum_k V_{ki} \right)^{1/3} + \left(\sum_k V_{kj} \right)^{1/3} \right]^2} \left[\frac{1}{M_i} + \frac{1}{M_j} \right]^{1/2} \tag{6}$$

In this equation, the pressure is in atm and the binary diffusion coefficient Dij is in [cm^2/s].
The values for $\left(\sum V_{ki} \right)$ are given by Fuller et al. [13].
The temperature field is obtained by solving the convective energy equation;

$$\nabla \cdot \left(r_g \left(\rho_g Cp_g \mathbf{u}_g T - k_g \nabla T \right) \right) = 0 \tag{7}$$

where Cp is specific heat capacity [J/(kg.K)], k is gas thermal conductivity [W/(m.K)].

The gas phase and the liquid phase are assumed to be in thermodynamic equilibrium; hence, the temperature of the liquid water is the same as the gas phase temperature.

2.2.2 Gas diffusion layers
The physics of multiple phases through a porous medium is further complicated here with phase change and the sources and sinks associated with the electrochemical reaction. The equations used to describe transport in the gas diffusion layers are given below. Mass transfer in the form of evaporation $\left(\dot{m}_{phase} > 0 \right)$ and condensation $\left(\dot{m}_{phase} < 0 \right)$ is assumed, so that the mass balance equations for both phases are;

$$\nabla \cdot \left((1 - sat)\rho_g \varepsilon \mathbf{u}_g \right) = \dot{m}_{phase} \tag{8}$$

$$\nabla \cdot \left(sat.\rho_l \varepsilon \mathbf{u}_l \right) = \dot{m}_{phase} \tag{9}$$

where *sat* is saturation, ε is porosity
The momentum equation for the gas phase reduces to Darcy's law, which is, however, based on the relative permeability for the gas phase (KP). The relative permeability accounts for the reduction in pore space available for one phase due to the existence of the second phase [14].
The momentum equation for the gas phase inside the gas diffusion layer becomes;

$$\mathbf{u}_g = -(1 - sat)Kp.\nabla P / \mu_g \tag{10}$$

where *KP* is hydraulic permeability [m^2].
Two liquid water transport mechanisms are considered; shear, which drags the liquid phase along with the gas phase in the direction of the pressure gradient, and capillary forces, which drive liquid water from high to low saturation regions [14]. Therefore, the momentum equation for the liquid phase inside the gas diffusion layer becomes;

$$\mathbf{u}_l = -\frac{KP_l}{\mu_l}\nabla P + \frac{KP_l}{\mu_l}\frac{\partial P_c}{\partial sat}\nabla sat \tag{11}$$

where *Pc* is capillary pressure [Pa].
The functional variation of capillary pressure with saturation is prescribed following Leverett [14] who has shown that;

$$P_c = \tau\left(\frac{\varepsilon}{KP}\right)^{1/2}\left(1.417(1 - sat) - 2.12(1 - sat)^2 + 1.263(1 - sat)^3\right) \tag{12}$$

where τ is surface tension [N/m].
The liquid phase consists of pure water, while the gas phase has multi components. The transport of each species in the gas phase is governed by a general convection-diffusion equation in conjunction which the Stefan-Maxwell equations to account for multi species diffusion;

$$\nabla \cdot \left[\begin{array}{l} -(1 - sat)\rho_g \varepsilon y_i \sum_{j=1}^{N} D_{ij} \frac{M}{M_j}\left[\left(\nabla y_j + y_j \frac{\nabla M}{M}\right) + (x_j - y_j)\frac{\nabla P}{P}\right] + \\ (1 - sat)\rho_g \varepsilon y_i \cdot \mathbf{u}_g + \varepsilon D_i^T \frac{\nabla T}{T} \end{array} \right] = \dot{m}_{phase} \tag{13}$$

In order to account for geometric constraints of the porous media, the diffusivities are corrected using the Bruggemann correction formula [15];

$$D_{ij}^{eff} = D_{ij} \times \varepsilon^{1.5} \tag{14}$$

The heat transfer in the gas diffusion layers is governed by the energy equation as follows;

$$\nabla \cdot \left((1 - sat)\left(\rho_g \varepsilon C p_g \mathbf{u}_g T - k_{eff,g} \varepsilon \nabla T \right) \right) = \varepsilon \beta (T_{solid} - T) - \varepsilon \dot{m}_{phase} \Delta H_{evap} \tag{15}$$

where *keff* is effective electrode thermal conductivity [W/(m·K)]; the term [εβ(Tsolid−T)], on the right hand side, accounts for the heat exchange to and from the solid matrix of the GDL. The gas phase and the liquid phase are assumed to be in thermodynamic equilibrium, i.e., the liquid water and the gas phase are at the same temperature.
The potential distribution in the gas diffusion layers is governed by;
$$\nabla \cdot (\lambda_e \nabla \phi) = 0 \tag{16}$$

where λe is electrode electronic conductivity [S/m].
In order to account for the magnitude of phase change inside the GDL, expressions are required to relate the level of over- and undersaturation as well as the amount of liquid water present to the amount of water undergoing phase change. In the present work, the procedure of Berning and Djilali [16] was used to account for the magnitude of phase change inside the GDL.

2.2.3 Catalyst layers
The catalyst layer is treated as a thin interface, where sink and source terms for the reactants are implemented. Due to the infinitesimal thickness, the source terms are actually implemented in the last grid cell of the porous medium. At the cathode side, the sink term for oxygen is given by;

$$S_{O_2} = -\frac{M_{O_2}}{4F} i_c \tag{17}$$

where F is Faraday's constant (96487 [C/mole]), *ic* is cathode local current density [A/m^2], M is molecular weight [kg/mole].
Whereas the sink term for hydrogen is specified as;

$$S_{H_2} = -\frac{M_{H_2}}{2F} i_a \tag{18}$$

where ia is anode local current density [A/m^2]
The production of water is modelled as a source terms, and hence can be written as;

$$S_{H_2O} = \frac{M_{H_2O}}{2F} i_c \tag{19}$$

The generation of heat in the cell is due to entropy changes as well as irreversibility's due to the activation overpotential [17];

$$\dot{q} = \left[\frac{T(-\Delta s)}{n_e F} + \eta_{act} \right] i \tag{20}$$

where $\dot{q}$ is heat generation [W/m^2], ne is number of electrons transfer, *s* is specific entropy [J/(mole.K)], ηact is activation overpotential (V).
The local current density distribution in the catalyst layers is modelled by the Butler-Volmer equation [18, 19];

$$i_c = i_{o,c}^{ref} \left(\frac{C_{O_2}}{C_{O_2}^{ref}} \right) \left[\exp\left(\frac{\alpha_a F}{RT} \eta_{act,c} \right) + \exp\left(-\frac{\alpha_c F}{RT} \eta_{act,c} \right) \right] \tag{21}$$

$$i_a = i_{o,a}^{ref} \left(\frac{C_{H_2}}{C_{H_2}^{ref}} \right)^{1/2} \left[\exp\left(\frac{\alpha_a F}{RT} \eta_{act,a} \right) + \exp\left(-\frac{\alpha_c F}{RT} \eta_{act,a} \right) \right] \tag{22}$$

where C_{H_2} is local hydrogen concentration [mole/m3], $C_{H_2}^{ref}$ is reference hydrogen concentration [mole/m3], C_{O_2} is local oxygen concentration [mole/m3], $C_{O_2}^{ref}$ is reference oxygen concentration [mole/m3], $i_{o,a}^{ref}$ is anode reference exchange current density, $i_{o,c}^{ref}$ is cathode reference exchange current density, R is universal gas constant (8.314 [J/(mole·K)]), αa is charge transfer coefficient, anode side, and αc is charge transfer coefficient, cathode side.

2.2.4 Membrane
The balance between the electro-osmotic drag of water from anode to cathode and back diffusion from cathode to anode yields the net water flux through the membrane;

$$N_W = n_d M_{H_2O} \frac{i}{F} - \nabla \cdot \left(\rho D_W \nabla c_W \right) \tag{23}$$

where Nw is net water flux across the membrane [kg/(m2·s)], n_d is electro-osmotic drag coefficient.
The water diffusivity in the polymer can be calculated as follow [20];

$$D_W = 1.3 \times 10^{-10} \exp\left[2416 \left(\frac{1}{303} - \frac{1}{T} \right) \right] \tag{24}$$

The variable c_W represents the number of water molecules per sulfonic acid group (i.e. $\mathrm{mol}\ H_2O / \mathrm{equivalent}\ SO_3^{-1}$). The water content in the electrolyte phase is related to water vapour activity via [21];

$$\begin{aligned}
c_W &= 0.043 + 17.81a - 39.85a^2 + 36.0a^3 & \left(0 < a \le 1 \right) \\
c_W &= 14.0 + 1.4(a-1) & \left(1 < a \le 3 \right) \\
c_W &= 16.8 & \left(a \ge 3 \right)
\end{aligned} \tag{25}$$

The water vapour activity a given by;
$$a = x_W P / P_{sat} \tag{26}$$

Heat transfer in the membrane is governed by;
$$\nabla \cdot \left(k_{mem} \cdot \nabla T \right) = 0 \tag{27}$$

where k_{mem} is membrane thermal conductivity [W/(m·K)].
The potential loss in the membrane is due to resistance to proton transport across membrane, and is governed by;

$$\nabla \cdot \left(\lambda_m \nabla \phi \right) = 0 \tag{28}$$

where λ_m is membrane ionic conductivity [S/m].

2.2.5 Hygro-Thermal stresses in fuel cell

Using hygrothermoelasticity theory, the effects of temperature and moisture as well as the mechanical forces on the behaviour of elastic bodies have been addressed. An uncoupled theory is assumed, for which the additional temperature changes brought by the strain are neglected. The total strain tensor of deformation, π, is the sum;

$$\pi = \pi_e + \pi_{pl} + \pi_T + \pi_S \tag{29}$$

where, π_e is the elastic strain component, π_{pl} is the plastic strain component, and π_T, π_S are the thermal and swelling induced strains, respectively.

The thermal strains resulting from a change in temperature of an unconstrained isotropic volume are given by;

$$\pi_T = \wp\left(T - T_{\mathrm{Re}f}\right) \tag{30}$$

where $\wp$ is thermal expansion [1/K].

The swelling strains caused by moisture change in membrane are given by;

$$\pi_S = \lambda_{mem}\left(\Re - \Re_{\mathrm{Re}f}\right) \tag{31}$$

where λ_{mem} is membrane humidity swelling-expansion tensor and $\Re$ is the relative humidity [%]. Following the work [22], the swelling-expansion for the membrane, λ_{mem}, is expressed as a polynomial function of humidity and temperature as follows;

$$\lambda_{mem} = \sum_{i,j=1}^{4} C_{ij} T^{4-i} \Re^{4-j} \tag{32}$$

where C_{ij} is the polynomial constants, see Ref. [22].

Assuming linear response within the elastic region, the isotropic Hooke's law is used to determine the stress tensor σ.

$$\sigma = \mathbf{G}\pi \tag{33}$$

where $\mathbf{G}$ is the constitutive matrix.

The effective stresses according to von Mises, 'Mises stresses', are given by;

$$\sigma_v = \sqrt{\frac{(\sigma_1 - \sigma_2)^2 + (\sigma_2 - \sigma_3)^2 + (\sigma_3 - \sigma_1)^2}{2}} \tag{34}$$

where σ_1, σ_2, σ_3 are the principal stresses.

The mechanical boundary conditions are noted in Figure 2. The initial conditions corresponding to zero stress-state are defined; all components of the cell stack are set to reference temperature 20 C, and relative humidity 35% (corresponding to the assembly conditions) [8, 23, 24]. In addition, a constant pressure of (1 MPa) is applied on the surface of lower graphite plate, corresponding to a case where the fuel cell stack is equipped with springs to control the clamping force [8, 23, 24].

3. Results and discussion

The governing equations were discretized using a finite-volume method and solved using CFD code. Stringent numerical tests were performed to ensure that the solutions were independent of the grid size. A computational quadratic mesh consisting of a total of 64586 nodes and 350143 meshes was found to

provide sufficient spatial resolution (Figure 3). The coupled set of equations was solved iteratively, and the solution was considered to be convergent when the relative error was less than 1.0×10^{-6} in each field between two consecutive iterations. The calculations presented here have all been obtained on a Pentium IV PC (3 GHz, 2 GB RAM), using Windows XP operating system.
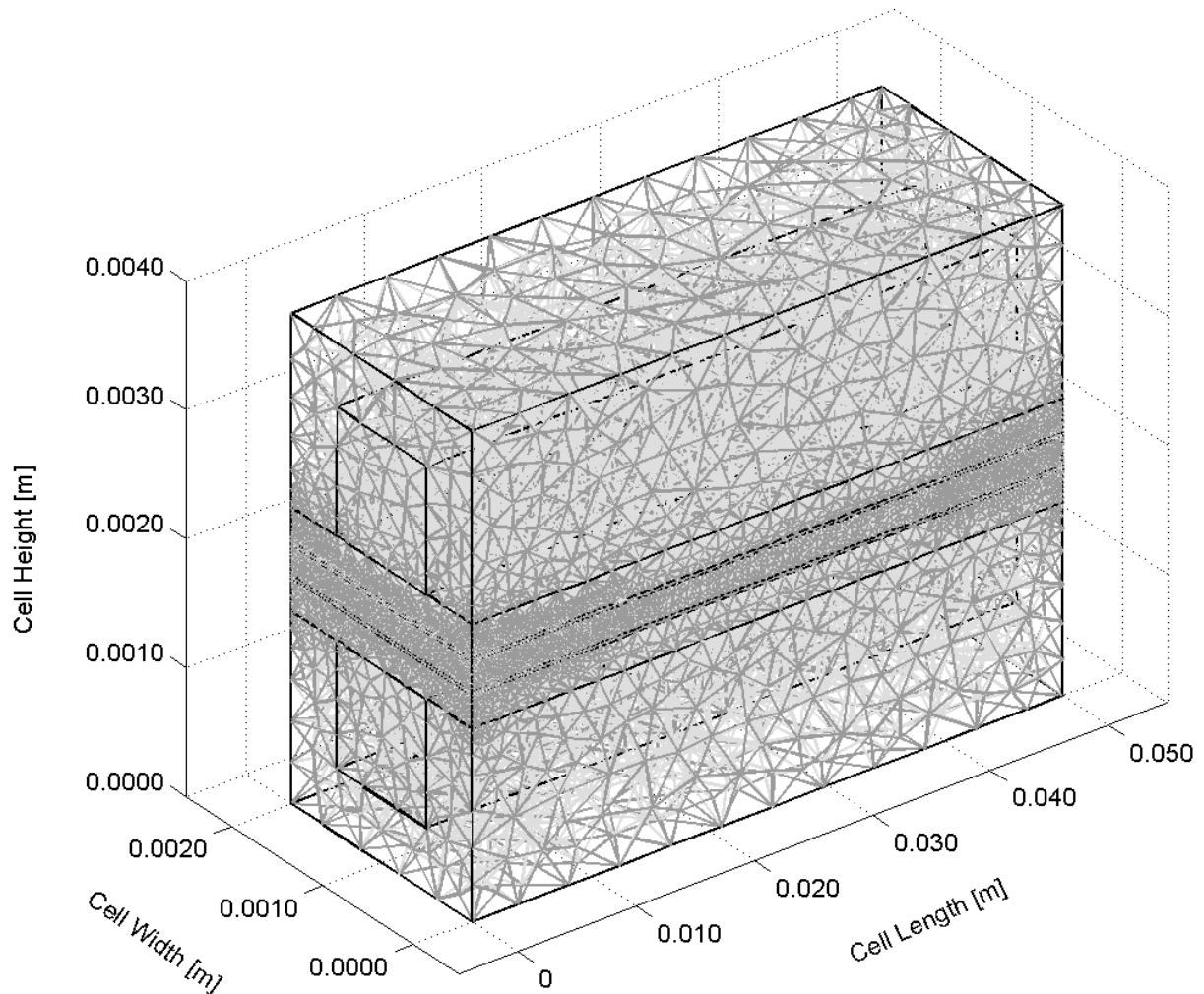
Figure 3. Computational mesh of a PEM fuel cell

The geometric and the base case operating conditions are listed in Table 1. Values of the electrochemical transport parameters for the base case operating conditions are taken from reference [11] and are listed in Table 2. The material properties for the fuel cell components used in this model are taken from reference [22] and are shown in Tables 3-5. The multi-phase model is validated by comparing model results to experimental data provided by Wang et al. [25]. Figure 4 shows the comparison of the polarization curves from the experimental data with the values obtained by the model at different operating fuel cell temperatures. It can be seen that the modelling results compare well with the experimental data. The importance of phase change to the accurate modelling of fuel cell performance is illustrated. Performance curves with and without phase change are also shown in Figure 4 for the base case conditions. Comparison of the two curves demonstrates that the effects of liquid water accumulation become apparent even at relatively low values of current density. Furthermore, when liquid water effects are not included in the model, the cell voltage dose not exhibit an increasingly steep drop as the cell approaches its limiting current density. This drop off in performance is clearly demonstrated by experimental data, but cannot be accurately modelled without the incorporation of phase change. By including the effects of phase change, the current model is able to more closely simulate performance, especially in the region where mass transport effects begin to dominate.
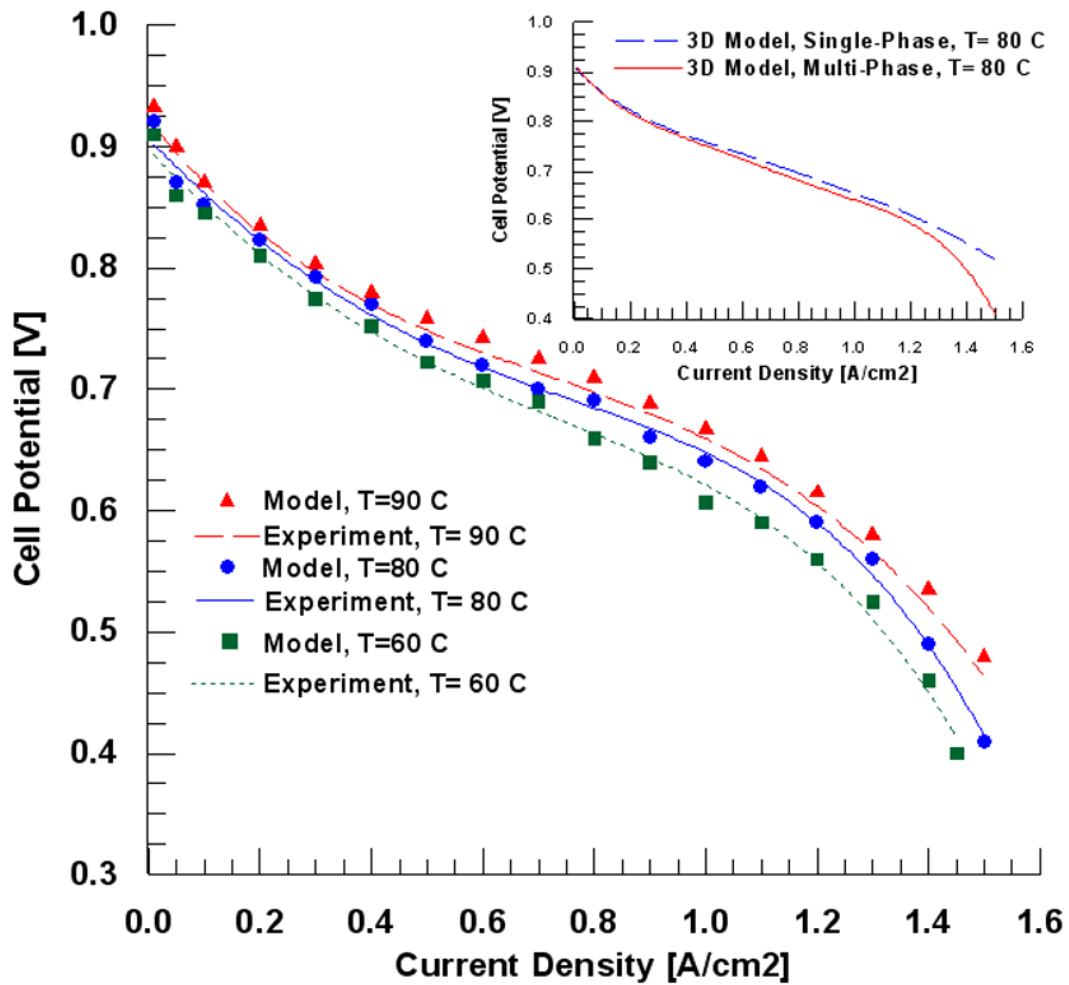
Figure 4. Comparison of the model and the experimental polarization curves

Table 1: Geometrical and operational parameters for base case conditions

Parameter	Symbol	Value
Channel length (X-direction)	L	0.05 m
Channel width (Y-direction)	W	1e-3 m
Channel height (Z-direction)	H	1e-3 m
Land area width	W_{land}	1e-3 m
Gas diffusion layer thickness	δ_{GDL}	0.26e-3 m
Wet membrane thickness (Nafion® 117)	δ_{mem}	0.23e-3 m
Catalyst layer thickness	δ_{CL}	0.0287e-3 m
Hydrogen reference mole fraction	$x_{H_2}^{ref}$	0.84639
Oxygen reference mole fraction	$x_{O_2}^{ref}$	0.17774
Anode pressure	P_a	3e5 Pa
Cathode pressure	P_c	3e5 Pa
Inlet fuel and air temperature	T_{cell}	353.15 K
Relative humidity of inlet fuel and air	ψ	100 %
Air stoichiometric flow ratio	ξ_c	2
Fuel stoichiometric flow ratio	ξ_a	2

Table 2: Electrode and membrane parameters for base case operating conditions

Parameter	Symbol	Value
Electrode porosity	ε	0.4
Electrode electronic conductivity	λ_e	100 S/m
Membrane ionic conductivity (Nafion®117)	λ_m	17.1223 S/m
Transfer coefficient, anode side	α_a	0.5
Transfer coefficient, cathode side	α_c	1
Cathode reference exchange current density	$i_{o,c}^{ref}$	1.8081e-3 A/m^2
Anode reference exchange current density	$i_{o,a}^{ref}$	2465.598 A/m^2
Electrode thermal conductivity	k_{eff}	1.3 W/m.K
Membrane thermal conductivity	k_{mem}	0.455 W/m.K
Electrode hydraulic permeability	kp	1.76e-11 m^2
Entropy change of cathode side reaction	ΔS	-326.36 J/mol.K
Heat transfer coef. between solid and gas phase	β	4e6 W/m^3
Protonic diffusion coefficient	D_{H^+}	4.5e-9 m^2/s
Fixed-charge concentration	c_f	1200 mol/m^3
Fixed-site charge	z_f	-1
Electro-osmotic drag coefficient	n_d	2.5
Droplet diameter	D_{drop}	1e-8 m
Condensation constant	C	1e-5
Scaling parameter for evaporation	ϖ	0.01

Table 3: Material properties used in the model

Parameter	Symbol	Value
Electrode Poisson's ratio	$\Im_{GDL}$	0.25
Membrane Poisson's ratio	$\Im_{mem}$	0.25
Electrode thermal expansion	$\wp_{GDL}$	-0.8e-6 1/K
Membrane thermal expansion	$\wp_{mem}$	123e-6 1/K
Electrode Young's modulus	Ψ_{GDL}	1e10 Pa
Membrane Young's modulus	Ψ_{mem}	Table 4
Electrode density	ρ_{GDL}	400 kg/m^3
Membrane density	ρ_{mem}	2000 kg/m^3
Membrane humidity swelling-expansion tensor	λ_{mem}	from eq.(32)

Table 4: Young's modulus at various temperatures and humidities of Nafion

Young's modulus [MPa]	Relative humidity [%]			
	30	50	70	90
T=25 C	197	192	132	121
T=45 C	161	137	103	70
T=65 C	148	117	92	63
T=85 C	121	85	59	46

Table 5: Yield strength at various temperatures and humidities of Nafion

Yield stress [MPa]	Relative humidity [%]			
	30	50	70	90
T=25 C	6.60	6.14	5.59	4.14
T=45 C	6.51	5.21	4.58	3.44
T=65 C	5.65	5.00	4.16	3.07
T=85 C	4.20	3.32	2.97	2.29

Thermal management is required to remove the heat produced by the electrochemical reaction in order to prevent drying out of the membrane and excessive thermal stresses that may result in rupture of the membrane [26]. The small temperature differential between the fuel cell stack and the operating environment make thermal management a challenging problem in PEM fuel cells. The temperature distribution inside the fuel cell has important effects on nearly all transport phenomena, and knowledge of the magnitude of temperature increases due to irreversibilities might help preventing membrane failure.

Temperature distribution for the low, intermediate and high load conditions are demonstrates in Figure 5. In addition, Figure 6 shows the temperature profiles in the through-plane direction where data taken at x=10 mm length of the cell cutting across the middle of the flow channel for multi-load conditions. In general, the temperature at the cathode side is higher than at the anode side, due to the reversible and irreversible entropy production. Naturally, the maximum temperature occurs, where the electrochemical activity is highest, which is near the cathode side inlet area. The temperature peak appears in the cathode catalyst layer, implying that major heat generation takes place in this region. In all loading conditions, the distributions of temperature are similar. However, the temperature increase for low load condition of 0.3 A/cm^2 is small, only 1.537 K. This is different for high nominal current density (1.2 A/cm^2). A much larger fraction of the current is being generated near the inlet of the cathode side at the catalyst layer and this leads to a significantly larger amount of heat being generated here. The maximum temperature is more than 7 K above the gas inlet temperature and it occurs inside the cathode catalyst layer.

The durability of proton exchange membranes used in fuel cells is a major factor in the operating lifetime of fuel cell systems. The Membrane-Electrode-Assembly (MEA) is the core component of PEM fuel cell and consists of membrane with the gas-diffusion layers including the catalyst attached to each side. Figure 7 shows stress distribution (contour plots) and total displacement (deformed shape plot, scale enlarged 200 times) inside the cell on the y-z plane at x=10 mm for three different nominal current densities. The figure illustrates the effect of stresses on the cell MEA. Because of the different thermal expansion and swelling coefficients between gas diffusion layers and membrane materials with non-uniform temperature distributions in the cell during operation, hygro-thermal stresses and deformation are introduced. The non-uniform distribution of stress, caused by the temperature gradient in cell MEA, induces localized bending stresses, which can contribute to delaminating between the membrane and the gas diffusion layers. It can be seen that the total displacement and the degree of the deformation in MEA are directly related to the temperature, where the temperature is highest in the centre of the channel and coincide with the highest reactant concentrations. In addition, the deformation that occurs in MEA under the land areas is much smaller than under the channel areas due to the clamping force effect.

The result shows that the maximum stress, the total displacement, and the degree of the deformation in MEA are directly related to the increasing of current density, due to increasing of heat generation. This result may explain the occurrence of cracks and pinholes in the membrane under steady–state loading during regular cell operation, especially at high load conditions.
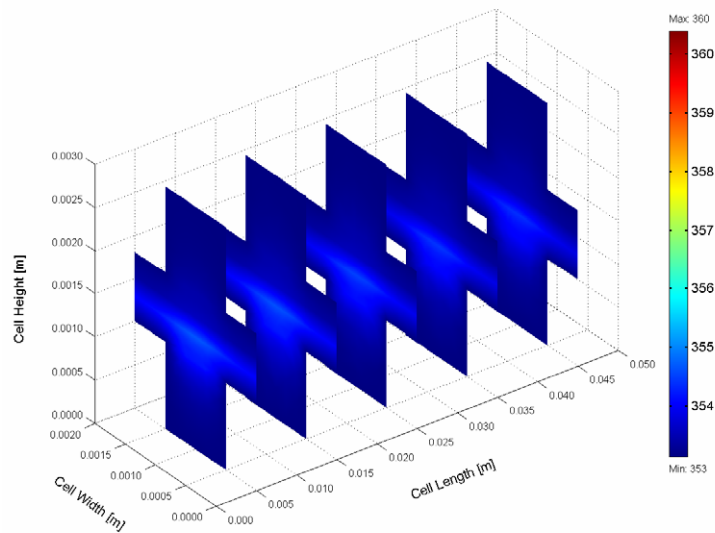
(a)
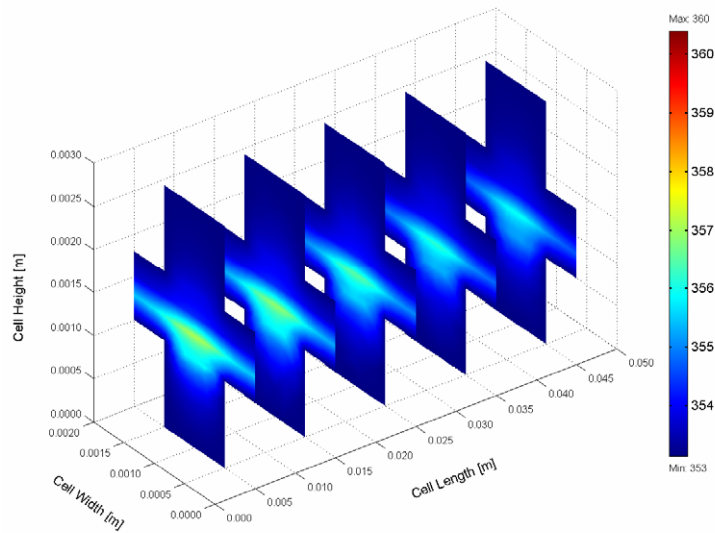
(b)
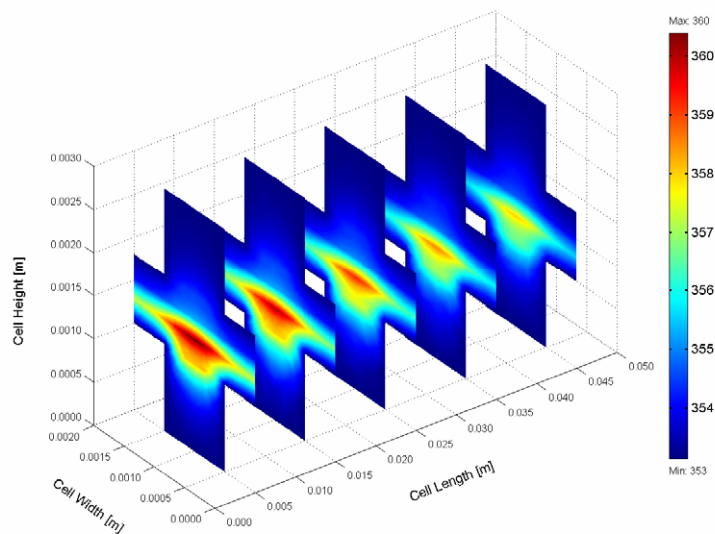
(c)

Figure 5. Temperature distribution inside the cell for three different nominal current densities: (a) 0.3 A/cm^2, (b) 0.7 A/cm^2, and (c) 1.2 A/cm^2
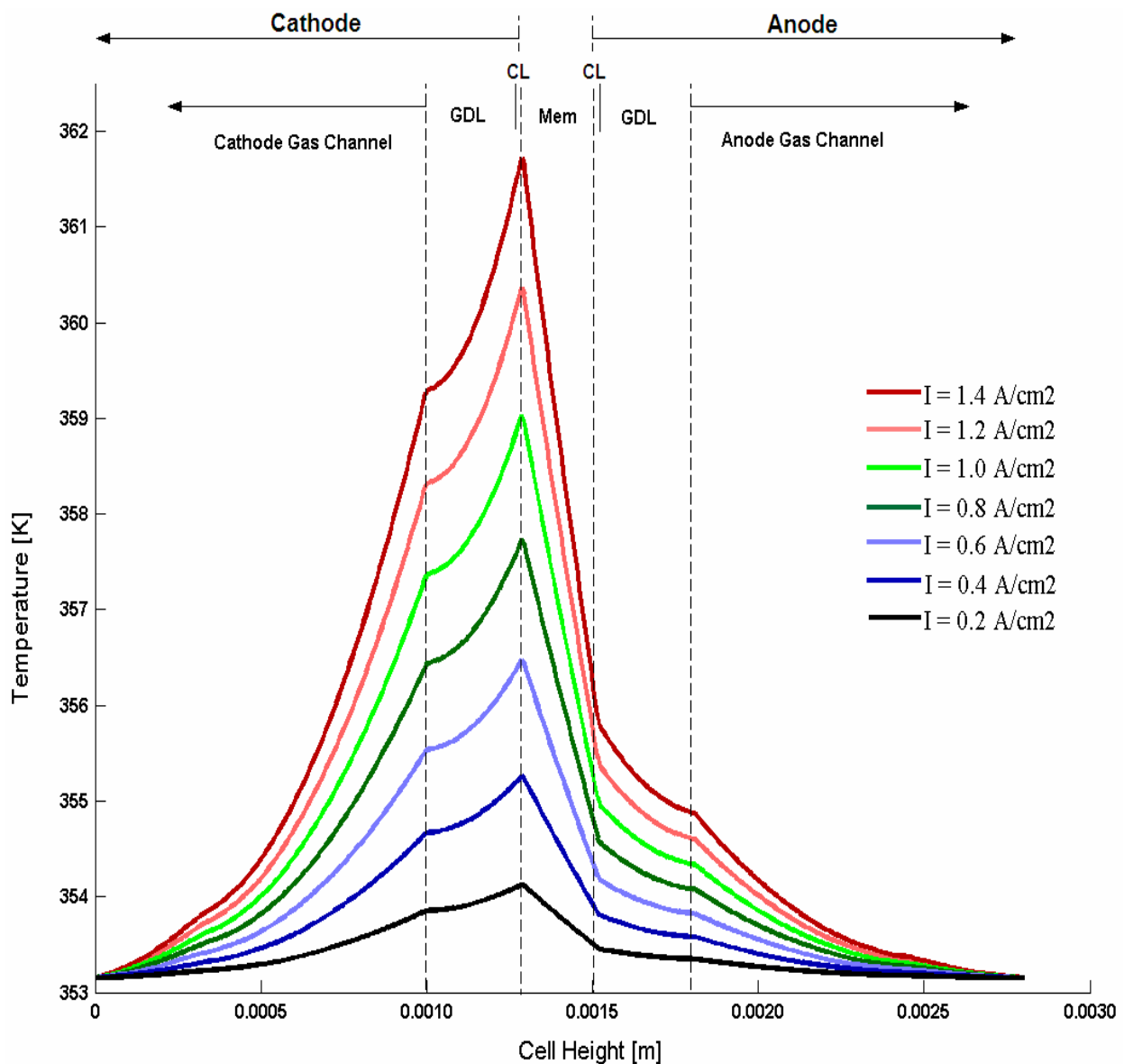
Figure 6. Temperature profiles along through-plane direction for multi-load conditions

Operating points (cell current) are based on defining specific system requirements, such as power level, voltage, efficiency, and system weight. Figure 8 shows the relationship between the thermodynamic efficiency and the power density of the cell operates at base case conditions. In addition, the figure shows the variation of the maximum temperature gradient inside the cell and the maximum mises stresses inside the MEA with cell power density. It is clearly shown that the efficiency at maximum power is much lower than the efficiency at partial loads, which makes the fuel cells very attractive and efficient for applications with highly variable loads where most of the time the fuel cell is operated at low load, low stresses, and high efficiency. The cell's nominal efficiency is therefore an arbitrary value, ranging anywhere between about 0.4 and ~ 0.7, which can be selected for any cell based on economic rather than on physical constraints.

However, since efficiency drops with increasing power density, there is a trade-off between high power and high efficiency. Fuel cell designers must select the desired operating range according to whether efficiency or power is paramount for the given application [27].
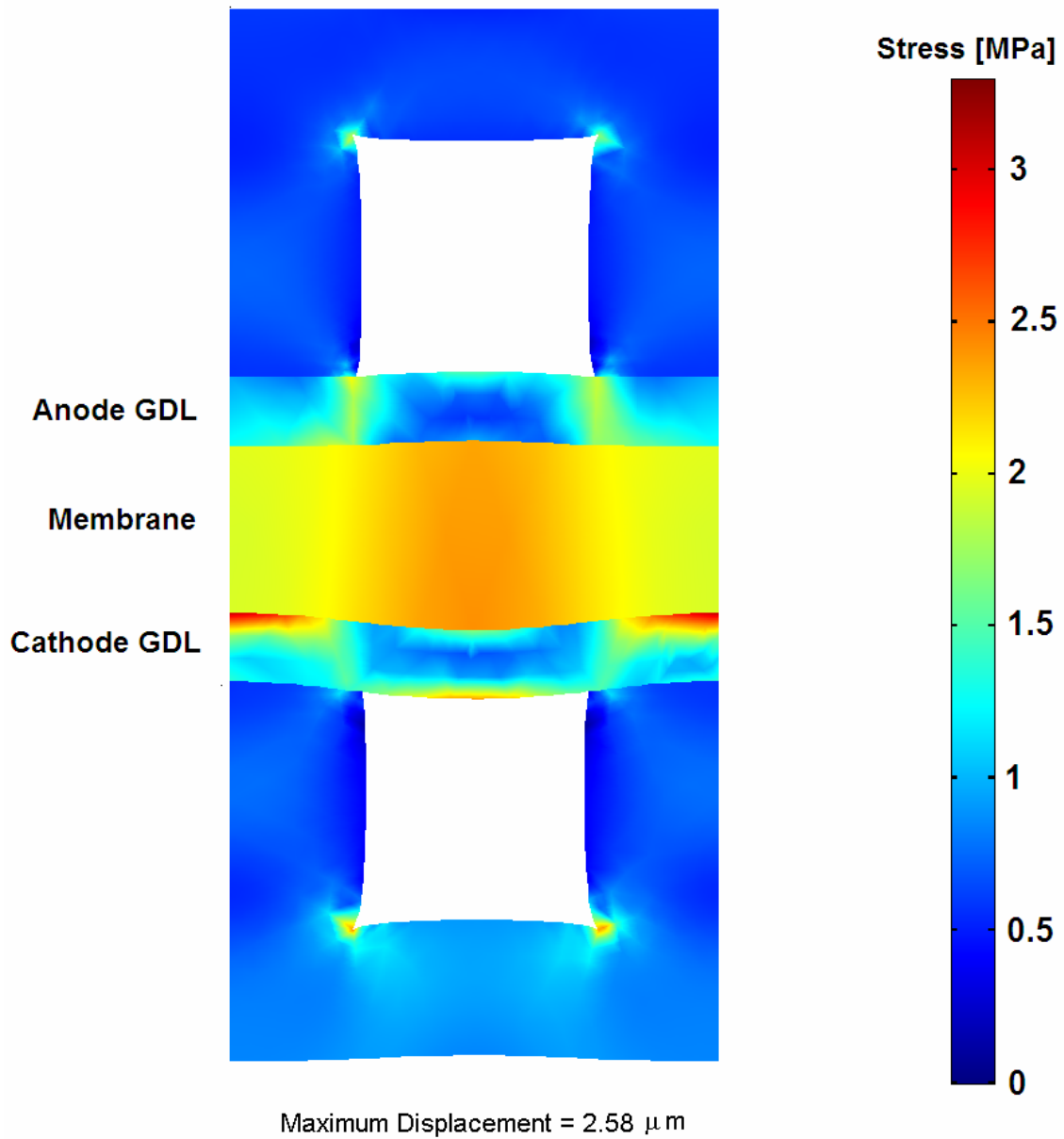
(a)

Figure 7. (Continued)
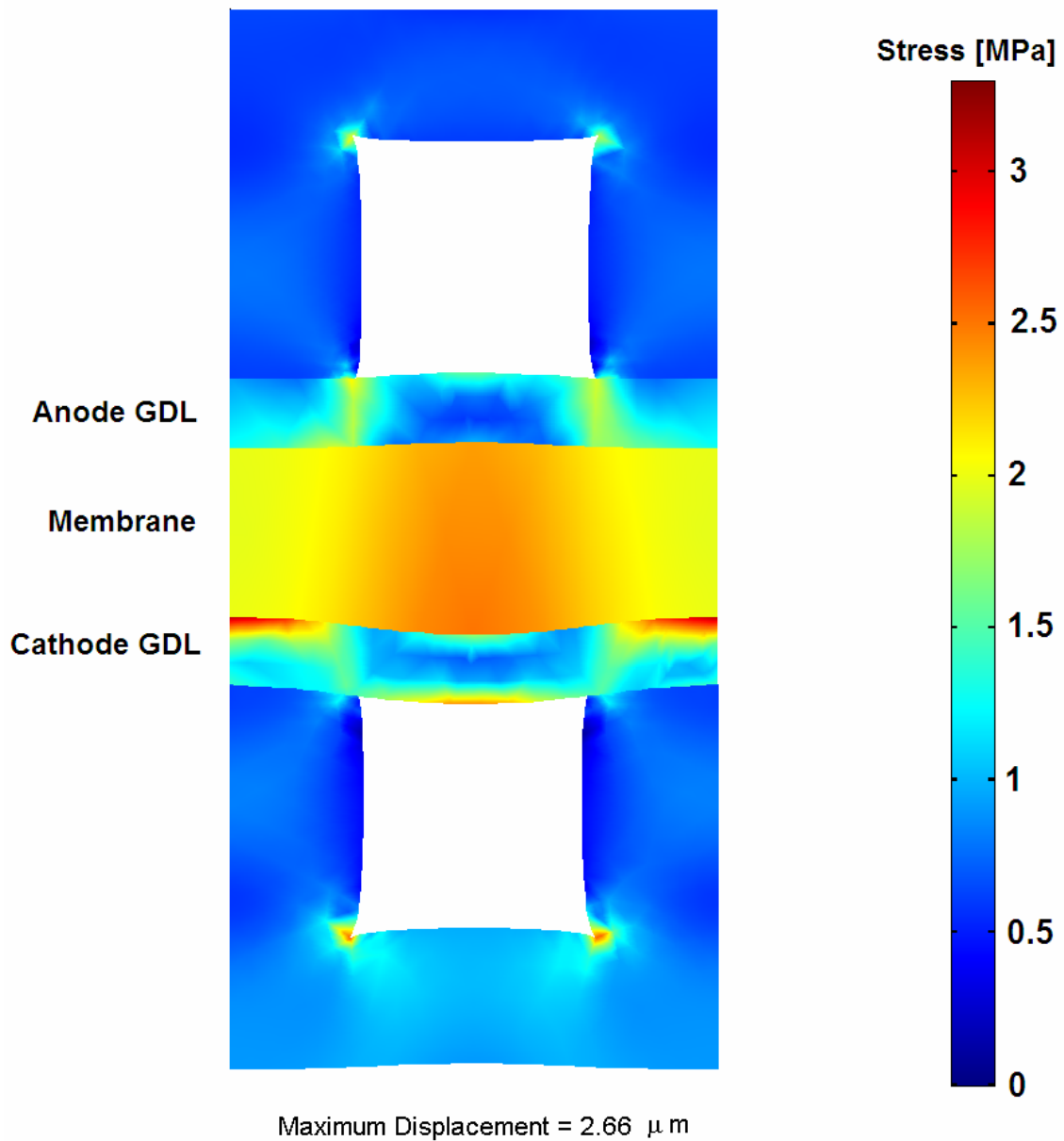
(b)

Figure 7. (Continued)

(c)
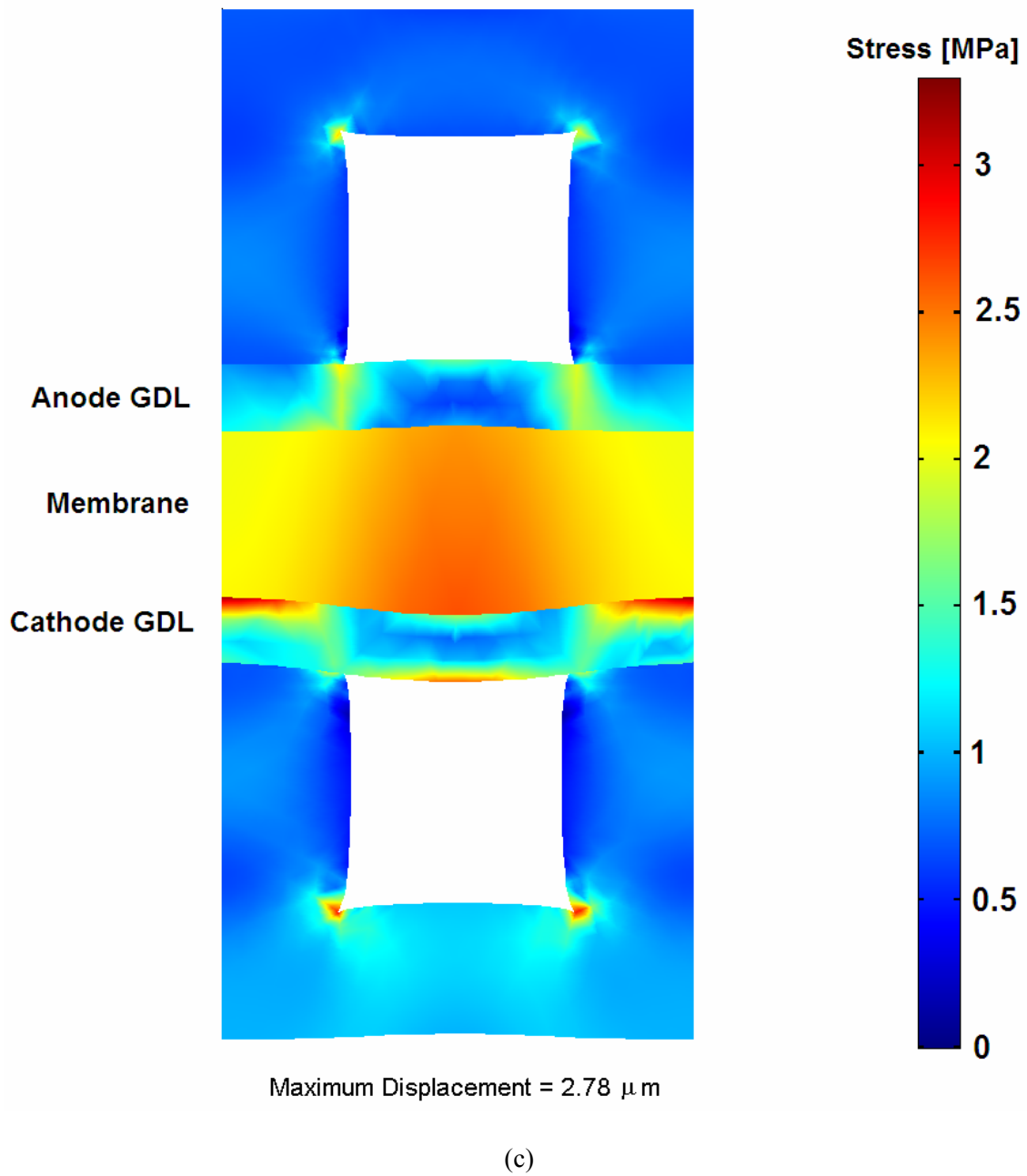
Figure 7. Von Mises stress distribution inside the cell (contour) and total displacement (deformed shape plot, scale enlarged 200 times) on the y-z plane at x=10 mm for three different nominal current densities: (a) 0.3 A/cm^2, (b) 0.7 A/cm^2, and (c) 1.2 A/cm^2
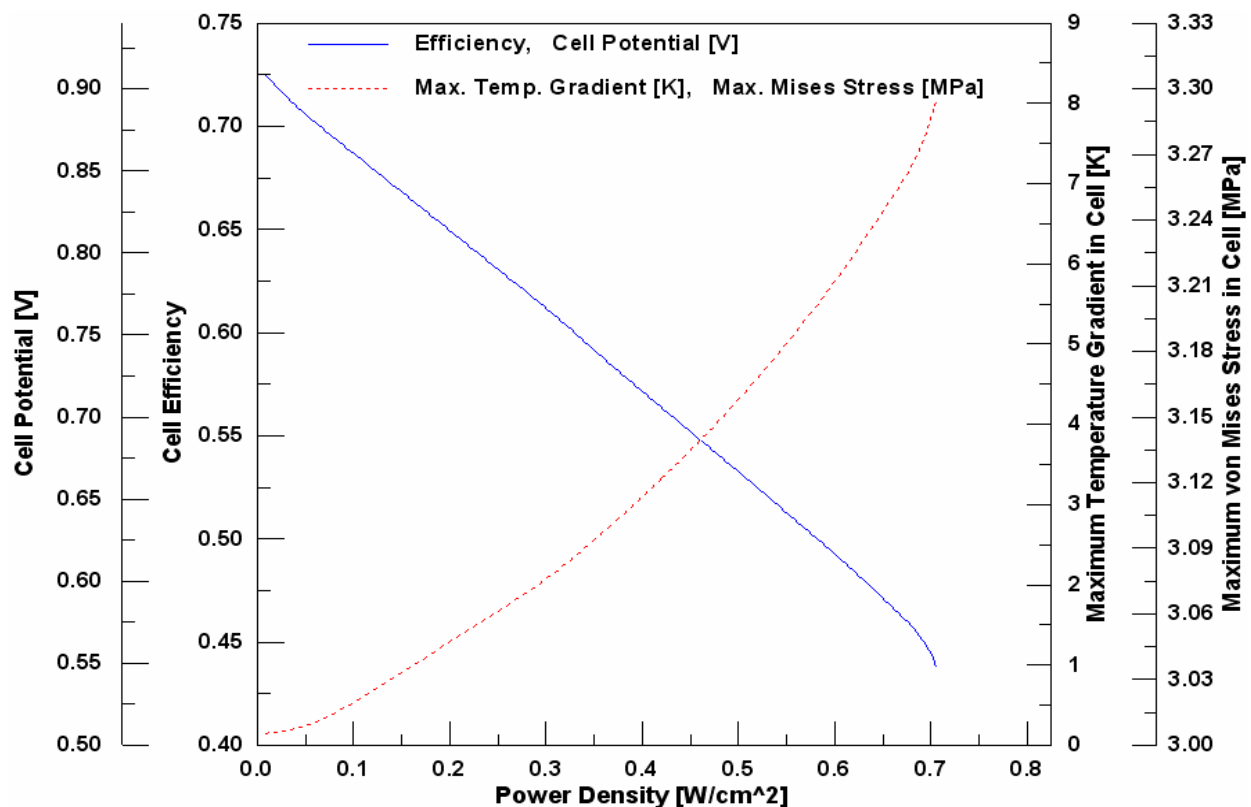
Figure 8. Relationship between the thermodynamic efficiency, the power density, and maximum stresses of the cell operates at base case conditions

4. Conclusion

A full three-dimensional, multi-phase computational fluid dynamics model of a PEM fuel cell has been developed to investigate the hygro-thermal stresses in PEM fuel cell, which developed during the cell operation due to the changes of temperature and relative humidity. A unique feature of the present model is to incorporate the effect of hygro and thermal stresses into actual three-dimensional fuel cell model. In addition, the temperature and humidity dependent material properties are utilize in the simulation for the membrane. The behaviour of the cell during operation has been studied and investigated under real operating conditions. The results show that the non-uniform distribution of stresses, caused by the temperature gradient in the cell, induces localized bending stresses, which can contribute to delaminating between the membrane and the gas diffusion layers. These stresses may explain the occurrence of cracks and pinholes in the membrane under steady–state loading during regular cell operation. The model is shown to be able to: (1) understand the many interacting, complex electrochemical and transport phenomena that cannot be studied experimentally; (2) identify limiting steps and components; and (3) provide a computer-aided tool for design and optimization of future fuel cell with much higher power density, long cell life, and lower cost.

In conclusion, the development of physically representative models that allow reliable simulation of the processes under realistic conditions is essential to the development and optimization of fuel cells, improve long-term performance and lifetime, the introduction of cheaper materials and fabrication techniques, and the design and development of novel architectures.

References
[1]   Zhang, S.; Yuan, X.; Wang, H.; Merida, W.; Zhu, H.; Shen, J.; Wu, S.; Zhang,J. A review of accelerated stress tests of MEA durability in PEM fuel cells. Int. J. Hydrogen Energy, 2009; 34(1): 388-404.
[2]   Wu, J.; Yuan, X.Z.; Martin, J.J.; Wang, H.; Zhang, J.; Shen, J.; Wu, S.; Merida, W. A review of PEM fuel cell durability: Degradation mechanisms and mitigation strategies. J. Power Sources, 2008; 184(1): 104-119.
[3]   Beuscher, U.; Cleghorn, S.J.C.; Johnson, W.B. Challenges for PEM fuel cell membranes. Int J Energy Res 2005; 29(12): 1103-1112.

[4]   Gode, P.; Ihonen, J.; Strandroth, A.; Ericson, H.; Lindbergh, G.; Paronen, M.; Sundholm, F.; Sundholm, G.; Walsby, N. Membrane durability in a PEM fuel cell studied using PVDF based radiation grafted membranes fuel cells. Fuel Cells 2003; 3(1-2): 21-27.

[5]   Maher A.R. Sadiq Al-Baghdadi. Mechanical behaviour of PEM fuel cell catalyst layers during regular cell operation. International Journal of Energy and Environment, 2010; 1(6), 927-936.

[6]   Stanic V, Hoberech M. Mechanism of pin-hole formation in membrane electrode assemblies for PEM fuel cells. Electrode Assemblies for PEM Fuel Cells, Electrochemical Society Inc., Pennington, NJ 08534-2896, United States, Honolulu, HI, United States, 2004; p. 1891.

[7]   Ramaswamy, N.; Hakim, N.; Mukerjee, S. Degradation mechanism study of perfluorinated proton exchange membrane under fuel cell operating conditions. Electroch Acta 2008; 53(8): 3279-3295.

[8]   Tang Y, Karlsson AM, Santare MH, Gilbert M, Cleghorn S, Johnson WB. An experimental investigation of humidity and temperature effects on the mechanical properties of perfluorosulfonic acid membrane. J Mater Sci Eng 2006; 425(1-2): 297-304.

[9]   Xie J, Wood DL, Wayne DM, Zawodzinski T, Borup RL. Durability of polymer electrolyte fuel cells at high humidity conditions. J Electrochem Soc 2005; 152(1): A104-A113.

[10]   Maher A.R. Sadiq Al-Baghdadi. A CFD analysis on the effect of ambient conditions on the hygro-thermal stresses distribution in a planar ambient air-breathing PEM fuel cell. International Journal of Energy and Environment, 2011; 2(4), 589-604.

[11]   Maher A.R. Sadiq Al-Baghdadi. Modeling optimizes PEM fuel cell durability using three-dimensional multi-phase computational fluid dynamics model. International Journal of Energy and Environment IJEE, 2010; 1(3), 375-398.

[12]   Suvorov, A.P.; Elter, J.; Staudt, R.; Hamm, R.; Tudryn, G.J.; Schadler, L.; Eisman, G. Stress relaxation of PBI based membrane electrode assemblies. Int. J. Solids and Structures, 2008; 45(24): 5987-6000.

[13]   Fuller, E.N.; Schettler, P.D.; Giddings, J.C. A new methode for prediction of binary gas-phase diffusion coefficients. Ind. Eng. Chem., 1966; 58(5): 18-27.

[14]   Berning, T.; Djilali, N. A 3D, multi-phase, multicomponent model of the cathode and anode of a PEM fuel cell. J. Electrochem. Soc., 2003; 150(12): A1589-A1598.

[15]   Nguyen, P.T.; Berning, T.; Djilali, N. Computational model of a PEM fuel cell with serpentine gas flow channels. J. Power Sources, 2004; 130(1-2): 149-157.

[16]   Berning T., Djilali N. A 3D, multi-phase, multicomponent model of the cathode and anode of a PEM fuel cell. J. Electrochem. Soc. 2003; 150(12): A1589-A1598.

[17]   Lampinen, M.J.; Fomino, M. Analysis of free energy and entropy changes for half-cell reactions. J. Electrochem. Soc., 1993; 140(12): 3537–3546.

[18]   Maher A.R. Sadiq Al-Baghdadi. Novel design of a compacted micro-structured air-breathing PEM fuel cell as a power source for mobile phones. International Journal of Energy and Environment IJEE, 2010; 1(4), 555-572.

[19]   Maher A.R. Sadiq Al-Baghdadi. Novel design of a disk-shaped compacted micro-structured air-breathing PEM fuel cell. International Journal of Energy and Environment, 2012; 3(2), 161-180.

[20]   Siegel, N.P.; Ellis, M.W.; Nelson, D.J.; von Spakovsky M.R. A two-dimensional computational model of a PEMFC with liquid water transport. J. Power Sources, 2004; 128(2): 173–184.

[21]   Hu, M.; Gu A.; Wang, M.; Zhu, X.; Yu, L.Three dimensional,two phase flow mathematical model for PEM fuel cell. Part I. Model development. Ener Conv Manage, 2004; 45(11-12): 1861-1882.

[22]   Kusoglu, A.; Karlsson, A.M., Santare, M.H.; Cleghorn, S.; Johnson, W.B. Mechanical behavior of fuel cell membranes under humidity cycles and effect of swelling anisotropy on the fatigue stresses. J. Power Sources, 2007; 170(2): 345-358.

[23]   Bograchev, D.; Gueguen, M.; Grandidier, J-C.; Martemianov, S. Stress and plastic deformation of MEA in running fuel cell. Int. J. Hydrogen Energy, 2008; 33(20): 5703–5717.

[24]   Product Information, DuPont™ Nafion® PFSA Membranes N-112, NE-1135, N-115, N-117, NE-1110 Perfluorosulfonic Acid Polymer. NAE101, 2005.

[25]   Wang L., Husar A., Zhou T., Liu H. A parametric study of PEM fuel cell performances. Int. J. Hydrogen Energy 2003; 28(11): 1263– 1272.

[26]   F.Brèque, J.Ramousse, Y.Dubé, K.Agbossou, P.Adzakpa. Sensibility study of flooding and drying issues to the operating conditions in PEM fuel cells. Int. J.of Energy & Env. IJEE,2010;1(1), 1-20

[27]   Maher A.R. Sadiq Al-Baghdadi. Optimal design of PEM fuel cells to generate maximum power: A CFD study. International Journal of Energy and Environment, 2011; 2(6), 953-962.